remote sensing

Article

Preflight Evaluation of the Environmental Trace Gases Monitoring Instrument with Nadir and Limb Modes (EMI-NL) Based on Measurements of Standard NO_2 Sample Gas

Taiping Yang [1], Fuqi Si [1,*], Haijin Zhou [1], Minjie Zhao [1], Fang Lin [1,2] and Lei Zhu [1]

[1] Key Laboratory of Environmental Optics and Technology, Anhui Institute of Optics and Fine Mechanics, Hefei Institutes of Physical Science, Chinese Academy of Sciences, Hefei 230031, China
[2] University of Science and Technology of China, Hefei 230026, China
* Correspondence: sifuqi@aiofm.ac.cn

Abstract: Hyperspectral observations are used to retrieve high-resolution horizontal distribution and vertical profiles of trace gases (O_3, NO_2, HCHO, and SO_2), thereby playing a vital role in monitoring the spatio-temporal distribution and transportation of atmospheric pollutants. These observations reflect air quality changes on global and regional scales, including China, thereby elucidating the impacts of anthropogenic and natural emissions on atmospheric composition and global climate change. The DaQi 02 (DQ02) satellite carries the Environmental Trace Gases Monitoring Instrument with Nadir and Limb modes (EMI-NL) onboard, which will simultaneously perform nadir and limb measurements of high-resolution ultraviolet and visible solar scattered light in the nadir and limb directions. Combined with the absorption of different trace gases in this wavelength band, this information can provide high-resolution horizontal and vertical distributions of trace gases. We examined the spectral measuring ability and instrument characteristics of both modules of EMI-NL by measuring different light sources and concentrations of the NO_2 sample gas. In the nadir module test, when the NO_2 sample gas concentration was 198 ppm and 513 ppm with scattered sunlight as the light source, the average relative errors of spatial pixels were 4.02% and 3.64%, respectively. At the NO_2 sample gas concentration of 198 ppm with the integrating sphere as the light source, the average relative error of spatial pixels was −2.26%. In the limb module test, when the NO_2 sample gas concentration was 198 ppm and 1000 ppm with the tungsten halogen lamp as the light source, the average relative errors of spatial pixels were −3.07% and 8.32%, respectively. When the NO_2 sample gas concentration was 198 ppm and 1000 ppm with the integrating sphere as the light source, the spatial pixel average errors were −3.5% and 8.06%, respectively. The retrieved NO_2 slant column density between different spatial pixels exhibited notable inconsistency in both modules, which could be used to estimate the stripe of spatial dimension. These results confirm the ability of EMI-NL to provide accurate spaceborne monitoring of NO_2 globally.

Keywords: environmental trace gases monitoring instrument with nadir and limb modules (EMI-NL); preflight evaluation; nadir module; limb module; NO_2

check for updates

Citation: Yang, T.; Si, F.; Zhou, H.; Zhao, M.; Lin, F.; Zhu, L. Preflight Evaluation of the Environmental Trace Gases Monitoring Instrument with Nadir and Limb Modes (EMI-NL) Based on Measurements of Standard NO_2 Sample Gas. *Remote Sens.* **2022**, *14*, 5886. https://doi.org/10.3390/rs14225886

Academic Editor: Hanlim Lee

Received: 19 September 2022
Accepted: 17 November 2022
Published: 20 November 2022

1. Introduction

Spaceborne hyperspectral remote sensing technology is widely used for monitoring global atmospheric pollution by measuring trace gases. Thus far, several key spaceborne instruments are used to monitor trace gases, including: the Total Ozone Mapping Spectrometer (TOMS), launched in 1978 onboard NIMBUS G [1]; the Global Ozone Monitoring Experiment (GOME), launched onboard the European Space Agency (ESA) ERS-2 satellite in 1995 [2]; the Scanning Imaging Absorption Spectrometer for Atmosphere Chartography (SCIAMACHY), launched in 2002 onboard the ESA Envisat satellite, which can achieve nadir, limb, and occultation observation function [3]; the Ozone Monitoring Instrument (OMI), launched onboard the National Aeronautics and Space Administration (NASA)

Earth Observing System (EOS) Aura satellite in 2004 [4]; GOME-2 [5]; and the Tropospheric Monitoring Instrument (TROPOMI), launched onboard the Sentinel-5 Precursor satellite in 2017 [6]. All these spaceborne instruments mainly reveal information on atmospheric transportation, atmospheric chemistry, and air pollutant emissions [7–15] through hyperspectral measurements.

In recent years, China has initiated the active development and application of hyperspectral observation technologies. Of such initiatives, the DaQi-02 satellite (DQ02) stands out as a new operational spaceborne system as part of a series of atmospheric observation satellites in China. Conceptually, DQ02 is a comprehensive detection satellite, aimed at meeting environmental management needs, namely, acquiring information about global climate change and atmospheric composition. From a technical standpoint, DQ02 is equipped with five types of remote sensing instruments: atmospheric detection lidar, a wide-range hyperspectral greenhouse gas monitor, infrared hyperspectral atmospheric composition detection, an ultraviolet hyperspectral atmospheric composition detector, and a cloud and aerosol imager. By exploiting these instruments, DQ02 will achieve large-scale, continuous, dynamic, and all-day comprehensive monitoring of atmospheric elements, such as greenhouse gases, gaseous pollutants, clouds, and aerosols by combining active and passive remote sensing techniques. Quality-assured observations from DQ02 will strengthen the technical capabilities of spaceborne monitoring in China by providing timely quantitative information on the ecological environment, natural resources, and agriculture.

The Environmental Trace Gases Monitoring Instrument with Nadir and Limb modes (EMI-NL) is one of the five payloads carried by DQ02, equipped with independent nadir and limb observations, mainly used to monitor the horizontal and vertical distribution of atmospheric trace gases. An instrument of the same series but only with a nadir observation mode, EMI [16], was launched in May 2018 and has been thereafter applied in numerous studies focused on trace gas and cloud parameter retrievals [17–23]. In particular, EMI02 [24] was launched in September 2021 with an equator-crossing time of 10:30 local time, and the DaQi-01 satellite (EMI03) was launched in April 2022. As mentioned, the EMI-NL onboard DQ02 should be launched in the following years, and the series of payloads will provide continuous observations, thereby reflecting horizontal and vertical distribution information of global atmospheric trace gases such as NO_2, SO_2, and O_3.

Most previous studies on the trace gas monitoring capability of spaceborne instruments before launch have normally relied on a xenon lamp. A xenon lamp allows the quantification of a trace gas in a gas cell at different temperatures and pressures [25–28]. For instance, the measurements of NO_2 and O_3 in a gas cell were carried out for OMI using a xenon lamp and zenith-scattered sunlight [29]. In this context, the spectral measurement capability of EMI can be evaluated by quantifying NO_2 in a sample gas cell using scattered sunlight in laboratory conditions [30]. Furthermore, the NO_2 slant column density (SCD) can be retrieved by the DOAS [31] algorithm.

To evaluate the trace gas measuring ability of EMI-NL, we measured the absorption spectrum of standard NO_2 sample gas with different concentrations in the gas cell for nadir and limb modules using different light sources in laboratory conditions. Specifically, the measured spectrum retrieved by the DOAS algorithm was utilized in our study to (a) evaluate the trace gas monitoring ability of spatial pixels of the nadir and limb modules of EMI-NL, and (b) investigate the cross-track stripe phenomenon of the EMI-NL spatial dimension.

2. Data and Methods

2.1. EMI-NL Description

EMI-NL is used to obtain high-resolution ultraviolet and visible scattered sunlight in the nadir and limb directions. The high-resolution trace gas horizontal and vertical distribution information is acquired using the absorption of different trace gases at this band. In this way, the quantitative monitoring of global atmospheric trace gas distribution and transportation is realized. The in-orbit observation schematic diagram of EMI-NL is illustrated in Figure 1, while the main parameters of EMI-NL are summarized in Table 1.

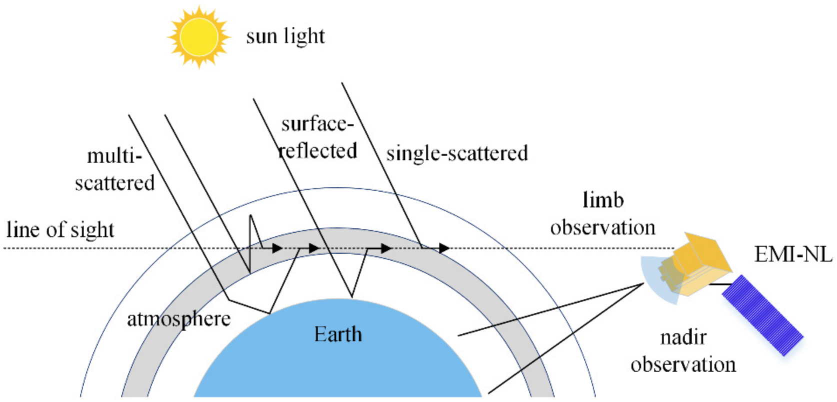

Figure 1. Diagram of EMI-NL in-orbit observation.

Table 1. EMI-NL instrumental properties.

	Nadir Module	Limb Module
Spectral channels	UV1: 300–400 nm, VIS1: 400–500 nm	UV1: 290–380 nm, UV2: 380–480 nm, VIS1:520–610 nm
Spectral resolution	$\leq$0.6 nm	
Telescope FOV	114° (cross-track)	$\geq$4.5° (horizontal direction)
Spatial resolution	$\leq$7 km (swath direction) × 7 km (flight direction)	$\leq$2 km (tangent direction)
CCD detectors	UV: 1022 × 954 (spectral × spatial) pixels VIS: 1022 × 954 (spectral × spatial) pixels	UV: 1024 × 1024 (spectral × spatial) pixels VIS: 1024 × 1024 (spectral × spatial) pixels
Mass	90 ± 0.9 kg	
orbit	Polar, sun-synchronous, ascending node equator crossing time: 13:30	

2.1.1. Nadir Module

The EMI-NL nadir module measures at the wavelength range of 300–500 nm, including two spectral channels of ultraviolet 1 and visible 1 (UV1: 300–400 nm, VIS1: 400–500 nm), using a Littrow–Offner convex grating imaging spectrometer, with the spectral resolution of 0.6 nm. Compared with the exclusive nadir geometries of EMI [1] and EMI-2 [18], the spatial resolution of the EMI-NL nadir module is substantially improved by providing 7 km (swath direction) × 7 km (flight direction) measurements. Moreover, its nadir module is characterized by a wide instantaneous field of view (IFOV) of 114° with a ground coverage of 2600 km in cross-orbit direction, thereby offering nearly a daily global coverage by observations.

The optical system block diagram of the EMI-NL nadir module is illustrated in Figure 2a. As seen, the light scattered and reflected from the Earth's atmosphere, or a surface is collected by the front telescope of the system and subsequently enters the relay optical system. The relay optical system splits the light using the color separation filter. Consequently, the light from each channel is reflected and converged into the corresponding Littrow–Offner imaging spectrometer. The imaging spectrometer has been designed using the Littrow–Offner structure, which facilitates the miniaturization adaptable for space technology. Finally, the dispersion in the spectrometer is imaged on the area-array CCD detector to obtain high spectral resolution and high spatial resolution spectral information.

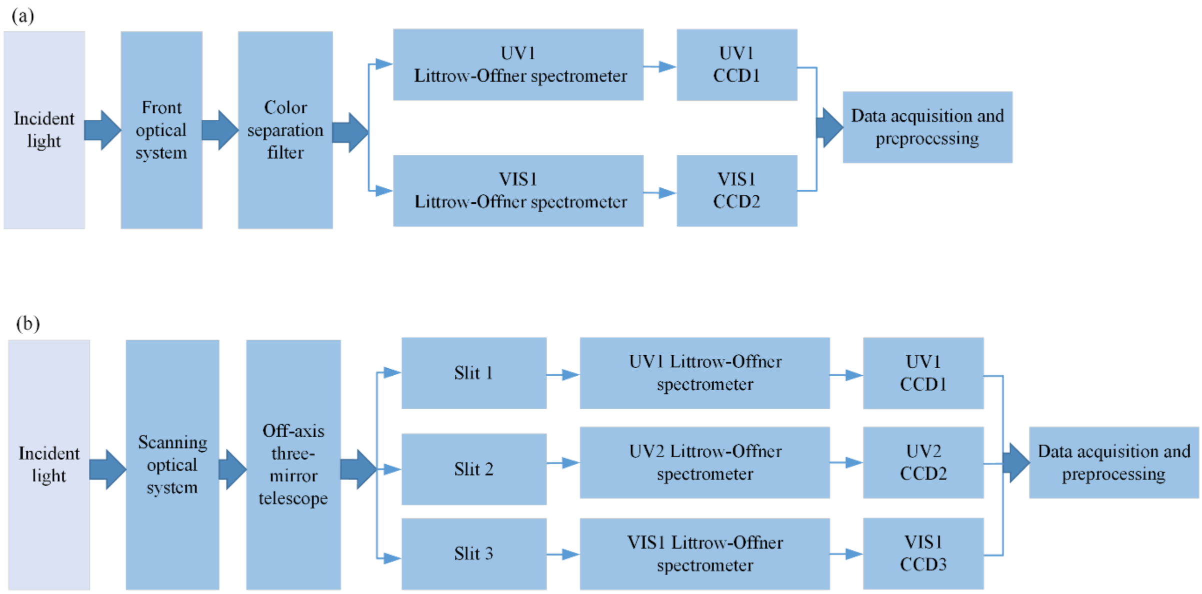

Figure 2. Optical system block diagram of the EMI-NL (**a**) nadir module and (**b**) limb module.

2.1.2. Limb Module

The wavelength range of the limb module of EMI-NL is 210–610 nm, including three channels: UV1 (290–380 nm), UV2 (380–480 nm), and VIS1 (520–610 nm) with a spectral resolution of 0.6 nm, and the spatial resolution in the tangent direction is 2 km. Notably, the limb observation method is a new observation approach in atmospheric remote sensing. In this method, the sunlight reflected by atmospheric molecules, aerosols, clouds, and the Earth's surface forms a 100 km thick limbic atmosphere around the Earth's periphery. The limb module measures the radiance of the limbic atmosphere to ultimately retrieve the high-altitude vertical distribution of trace gases and atmospheric aerosols. The retrieval is based on analyzing the spectral radiation characteristics of the limbic atmosphere.

Figure 2b displays the optical block diagram of the EMI-NL limb module. The scanning mirror guides the light into the front optical system, the off-axis three-mirror telescope performs the telephoto imaging, and the color separation filter splits light, thereby ultimately forming three independent spectral detection channels. The limb spectral information is gathered into the slit of each channel's imaging spectrometer. At the final stage, the condensed light of the front telephoto imaging system enters their channel's imaging spectrometer, disperses, and images to the area array CCD detector, thereby retrieving spectral imaging information in this way.

2.2. Experimental Design

The measurement of standard NO_2 sample gas in a cell was carried out for EMI-NL under the standard atmospheric pressure and temperature of 20 °C. The measurement was performed in the laboratory at the experimental observation field of the Anhui Institute of Optics and Fine Mechanics (located at 117.18°E, 31.9°N). Due to this fact, four sets of measurements were performed in the experiment: (1) the EMI-NL nadir module was evaluated with the scattered sunlight and the NO_2 sample gas concentrations with the mixing ratios of 198 and 513 parts per million (ppm) respectively; (2) the EMI-NL nadir module measurements were performed with the integrating sphere as the light source with the NO_2 sample gas concentration of 198 ppm; (3) the EMI-NL limb module was measured using the tungsten halogen lamp with the NO_2 sample gas concentration of 198 and 1000 ppm, respectively; and (4) while the EMI-NL limb module was measured using integrating sphere with the NO_2 sample gas concentration of 198 and 1000 ppm, respectively. The NO_2 sample gas concentration of 198 ppm is close to the high concentration of NO_2 SCD in the actual atmosphere; higher concentrations (513 ppm and 1000 ppm) of the NO_2

sample gas are good for DOAS fitting and accurate evaluation of EMI-NL. The schematic of the experimental setup is illustrated in Figure 3. As seen, the scattered sunlight entered the laboratory from the quartz glass window, passed through the sample gas cell (the sample gas cell length = 8 cm), and was ultimately measured by EMI-NL. The integrating sphere light source directly passed through the sample gas cell and was also ultimately measured by EMI-NL. During the experiment, the N_2 sample gas was first flushed for a few minutes to remove other gases from the sample gas cell and was subsequently filled with the NO_2 sample gas at a 6 L/min rate. Note that the entire field of view of EMI-NL nadir and limb modules was tested in this experiment.

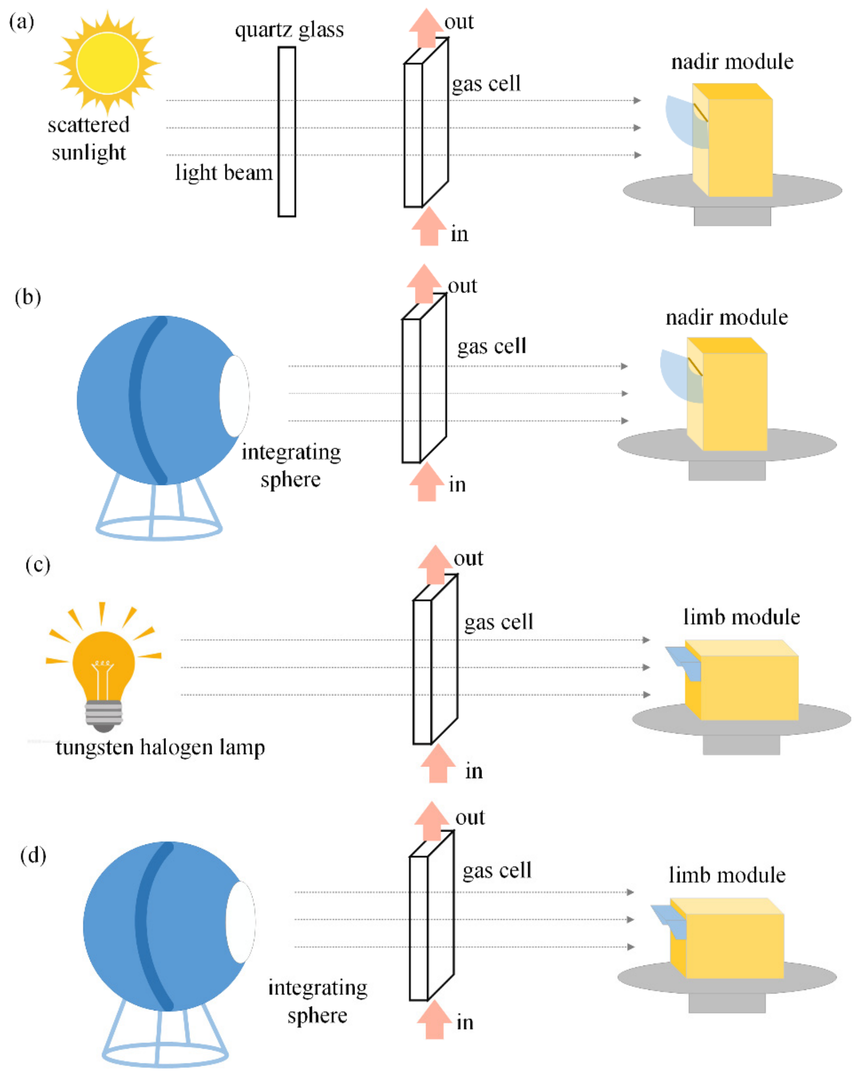

Figure 3. Schematic of the EMI-NL NO_2 sample gas measurement experimental setup. (**a**) EMI-NL nadir module measurements with the scattered sunlight; (**b**) EMI-NL nadir module measurements with the integrating sphere; (**c**) EMI-NL limb module measurements with the tungsten halogen lamp; (**d**) EMI-NL limb module measurements with integrating sphere.

2.3. DOAS Fitting

The spectrum measured by flushing the gas cell with the N_2 sample gas was utilized as the reference spectrum, whereas the NO_2 SCD was retrieved by the DOAS algorithm using the previously measured NO_2 sample gas spectrum. In this study, the fitting interval of the visible band 430–470 nm was applied. All these relevant parameter settings are summarized in Table 2. Zhang et al., (2018) [30] have previously outlined that by adding a ring cross section, one only negligibly affects DOAS spectral fitting results for laboratory sample gas measurement. On this basis, we did not add the ring cross section here. The DOAS algorithm can be formalized by Equation (1).

$$\ln\left[\frac{I_{N_2}(\lambda)}{I_{NO_2}(\lambda)}\right] = \sigma_{NO_2}(\lambda)S_{NO_2} + P(\lambda) \quad (1)$$

Table 2. NO_2 DOAS fit settings.

Parameter	Data Source
NO_2	NO_2 at 298 K [32]
Polynomial	5th
Fitting interval	430–470 nm

$I_{N2}(\lambda)$ and $I_{NO2}(\lambda)$ are the measured spectral when the gas cell is filled with N_2 and NO_2 sample gas, respectively, $\sigma_{NO2}(\lambda)$ is the NO_2 absorption cross section, S_{NO2} is the NO_2 SCD, and $P(\lambda)$ is the polynomial. Figure 4 shows an example of DOAS fitting in the nadir module of the 102nd pixel when the NO_2 sample gas concentration was 198 ppm and scattered sunlight was used.

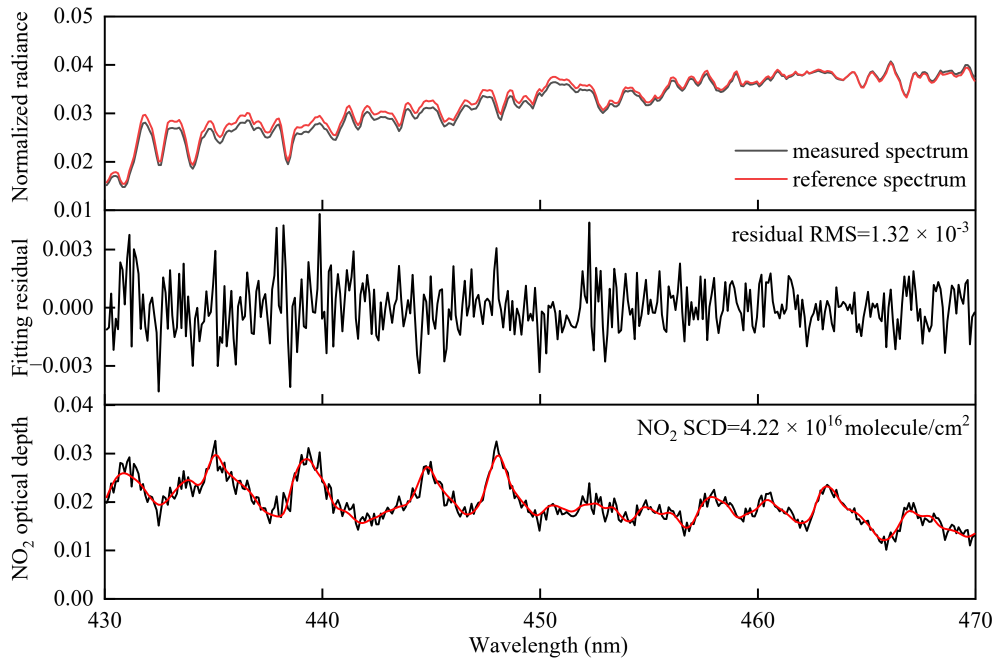

Figure 4. An example of NO_2 DOAS fitting of the measurement of the 102nd pixel of the nadir module as the NO_2 sample gas concentration is 198 ppm using scattered sunlight.

2.4. Signal-to-Noise Ratio Estimation

The signal-to-noise ratio (SNR) is a key indicator reflecting the ability of imaging spectroscopy to acquire effective target information. In particular, the magnitude of SNR reflects the detection limit monitoring ability of EMI-NL, which directly affects the quality of level 2 product retrieval calculation. The noise in the SNR is usually characterized by the standard deviation in statistics, and the SNR is usually calculated by continuous measurement and statistics with a stable light source at a certain brightness under laboratory conditions. Thus, thorough evaluation and determination of SNR are key steps in spaceborne imaging spectrometry. This study used the measurement spectrum using tungsten halogen lamps in the laboratory and treated the average value of 100 repeated spectral measurements at a wavelength of λ as the signal, while the standard deviation was used as the noise. Lastly, the ratio of signal and noise was defined as the SNR [16] at the wavelength λ according to Equations (2)–(4) below:

$$\text{SNR} = \frac{\text{signal}}{\text{noise}}. \tag{2}$$

$$\text{signal} = \sum_{i=1}^{100} I_i(\lambda). \tag{3}$$

$$\text{noise} = \sqrt{\frac{\sum_{i=1}^{100}\left(I_i(\lambda) - \overline{I(\lambda)}\right)^2}{99}}. \tag{4}$$

3. Results and Discussion

3.1. Results of the Nadir Module

The spatial row pixels 1–203 of the nadir module were measured in the experimental setup, as shown in Figure 3a. Note that the NO_2 SCD of the NO_2 sample gas was estimated based on the NO_2 volume mixing ratio and the length of the gas cell. At the concentrations of 198 ppm and 513 ppm, the NO_2 SCDs were found to be 3.92×10^{16} molecule/cm^2 and 1.01×10^{17} molecule/cm^2, respectively. Figure 5a demonstrates NO_2 SCD with fitting error and relative deviation of different spatial pixels when the flushed NO_2 sample gas was 198 ppm. As seen, the averaged NO_2 SCD of spatial pixels was $(4.08 \pm 0.14) \times 10^{16}$ molecule/cm^2 ($\pm 0.14 \times 10^{16}$ molecule/cm^2 is the averaged NO_2 SCD fitting error of spatial pixels), while the NO_2 SCD standard deviation of spatial pixels was 2.69×10^{15} (see Table 3). Compared with the estimated NO_2 SCDs, the average relative error of spatial pixels is 4.02%. Figure 5b shows that NO_2 SCD when the cell flushed NO_2 sample gas was 513 ppm. The averaged NO_2 SCD of spatial pixels was $(1.05 \pm 0.02) \times 10^{17}$ molecule/cm^2, and the NO_2 SCD standard deviation was 4.47×10^{15}. Figure 3b shows the measurement setup using an integrating sphere. The NO_2 SCD of the spatial pixels 1–190 is displayed in Figure 6 when the sample gas cell was filled with the 198 ppm NO_2 sample gas. Note that the NO_2 SCD of other spatial pixels 191–203 was not plotted due to the large observation elevation angle resulting in the radiance of these pixels being too low. Moreover, the averaged NO_2 SCD of spatial pixels was $(3.83 \pm 0.04) \times 10^{16}$ molecule/cm^2, and the standard deviation was 4.28×10^{14}. Figure 6 also shows that the retrieved NO_2 SCD between different spatial pixels exhibited notable inconsistency. Note that the possible drivers behind this inconsistency have been previously elaborated in detail by Zhang et al., (2018) [30]. The inconsistency could be caused by the influence of the low transmittance of quartz glass, which may have been triggered by the incomplete correction of the instrument's spatial pixels wavelength correction, slit function, dark current compensation, stray light correction, etc. Alternatively, the inconsistency could be driven by the stripe phenomenon of the two-dimensional CCD. In the experimental setup (1), the NO_2 sample gas concentrations were 198 and 513 ppm, while the variation trend of retrieved NO_2 SCD and relative deviation of different spatial pixels were fairly consistent, with the scattered sunlight applied. However, they were strikingly inconsistent when the integrating sphere was used as a light source. Consequently, the averaged NO_2 fitting error of integrating sphere was markedly lower than that of scattered sunlight when the NO_2 sample gas concentration was 198 ppm. This finding indicates that different spatial pixels responded differently to different light sources. In turn, this induces the emergence of different fitting errors, potentially triggered by the inconsistency of the light source.

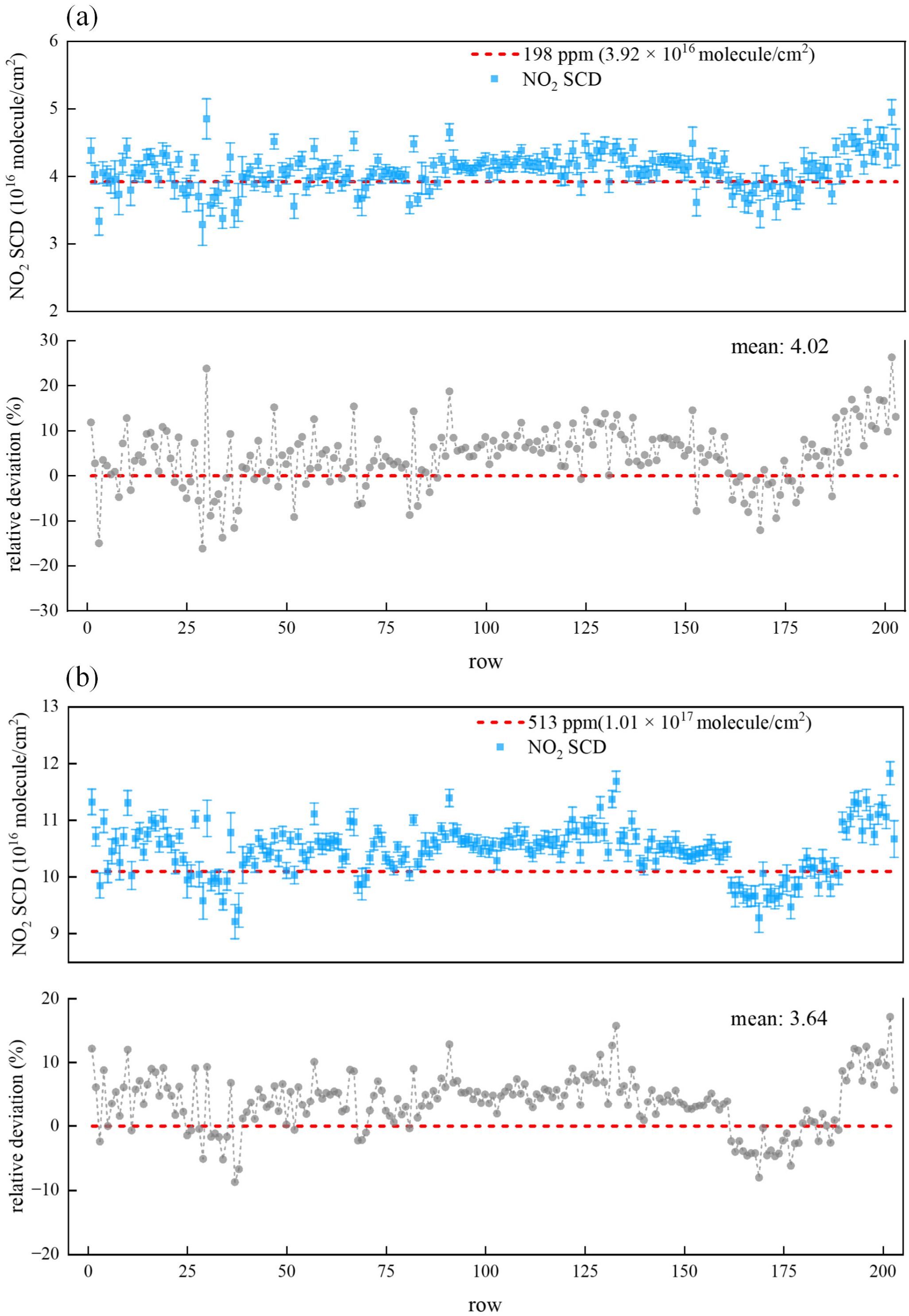

Figure 5. NO_2 SCD with fitting error and relative deviation of different spatial pixels of the EMI-NL nadir module with scattered sunlight and NO_2 sample gas concentrations of: (**a**) 198; and (**b**) 513 ppm.

Table 3. NO_2 gas cell measurement results of the nadir module.

Reference Spectral	NO_2 Gas (ppm)	Averaged NO_2 SCD (molecule/cm^2)	Standard Deviation of NO_2 SCD	Averaged NO_2 Fitting Error (molecule/cm^2)	Standard Deviation of NO_2 Fitting Error
Scattered sunlight	198	4.08×10^{16}	2.69×10^{15}	1.40×10^{15}	4.67×10^{14}
	513	1.05×10^{17}	4.47×10^{15}	1.59×10^{15}	4.96×10^{14}
Integrating sphere light	198	3.83×10^{16}	2.27×10^{15}	4.28×10^{14}	7.86×10^{13}

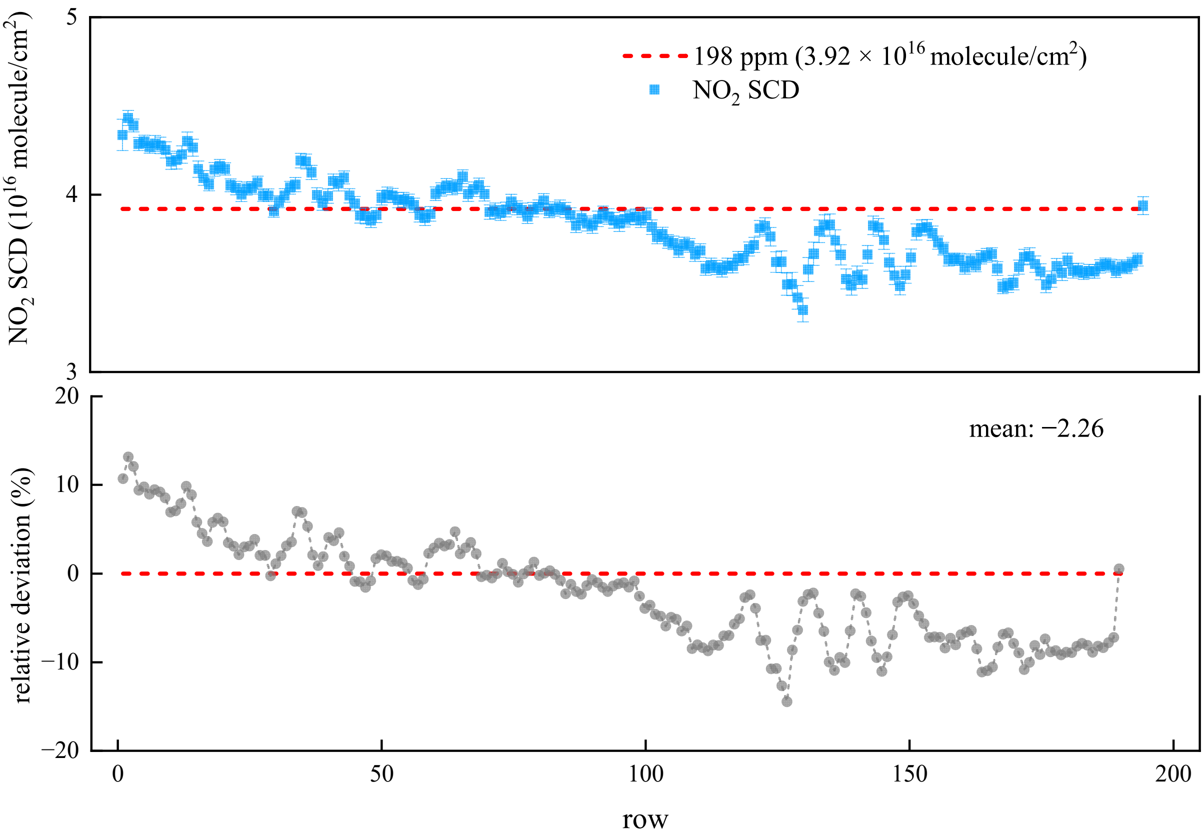

Figure 6. NO_2 SCD with fitting error and relative deviation of different spatial pixels of the EMI-NL nadir module with integrating sphere and an NO_2 sample gas concentration of 198 ppm.

3.2. Results of Limb Module

In the experimental setup, shown in Figure 3c, the spatial pixels 1–237 of the limb module were measured using the tungsten halogen lamp as a light source. When the NO_2 sample gas concentration was 198 ppm and 1000 ppm, the estimated NO_2 SCDs were 3.92×10^{16} molecule/cm^2 and 1.98×10^{17} molecule/cm^2, respectively. As shown in Figure 7a, when the flushed NO_2 sample gas is 198 ppm, the NO_2 SCD with fitting error and relative deviation of different spatial pixels are plotted. The average NO_2 SCD of spatial pixels was $(3.64 \pm 0.15) \times 10^{16}$ molecule/cm^2, while the standard deviation was 2.48×10^{15}, as seen in Table 4. Figure 7b shows the NO_2 SCD when the cell flushed NO_2 sample gas was 1000 ppm. Furthermore, the average NO_2 SCD of spatial pixels was $(2.06 \pm 0.02) \times 10^{17}$ molecule/cm^2, and the NO_2 SCD standard deviation was 4.27×10^{15}. The measurement using integrating sphere in the setup, shown in Figures 3d and 8a demonstrate that NO_2 SCD of spatial pixels at the sample gas cell was filled with 198 ppm NO_2 sample gas. Moreover, the average NO_2 SCD of spatial pixels was $(3.69 \pm 0.05) \times 10^{16}$ molecule/cm^2, and the standard deviation was 8.32×10^{14}. Figure 8b shows the retrieved NO_2 SCD when the NO_2 sample gas was 1000 ppm. The average NO_2 SCD of spatial pixels was $(2.04 \pm 0.01) \times 10^{17}$ molecules/cm^2, and the NO_2 SCD standard deviation was 1.7×10^{15}. The same figure also indicates that the retrieved NO_2 SCD exhibited remarkable inconsistency between the different spatial pixels, while the fitting error of the integrating sphere was significantly smaller, compared to that of the tungsten halogen lamp. Moreover, at the NO_2 sample gas concentration was 198 ppm, regardless of the light source (the tungsten halogen lamp or the integrating sphere), the average NO_2 SCD of spatial pixels was underestimated by −3.07% and −3.5%, respectively. When the sample gas concentration was 1000 ppm, NO_2 SCD was overestimated by 8.32% and 8.06%, respectively. This may be caused by the characteristics of the instrument itself or the unstable control of the sample gas flushing rate. It should also be noted that such spatial pixel-dependent error can be regarded as the error evaluation and can therefore be utilized for correcting the NO_2 SCD stripe [33–35] in the actual in-orbit monitoring.

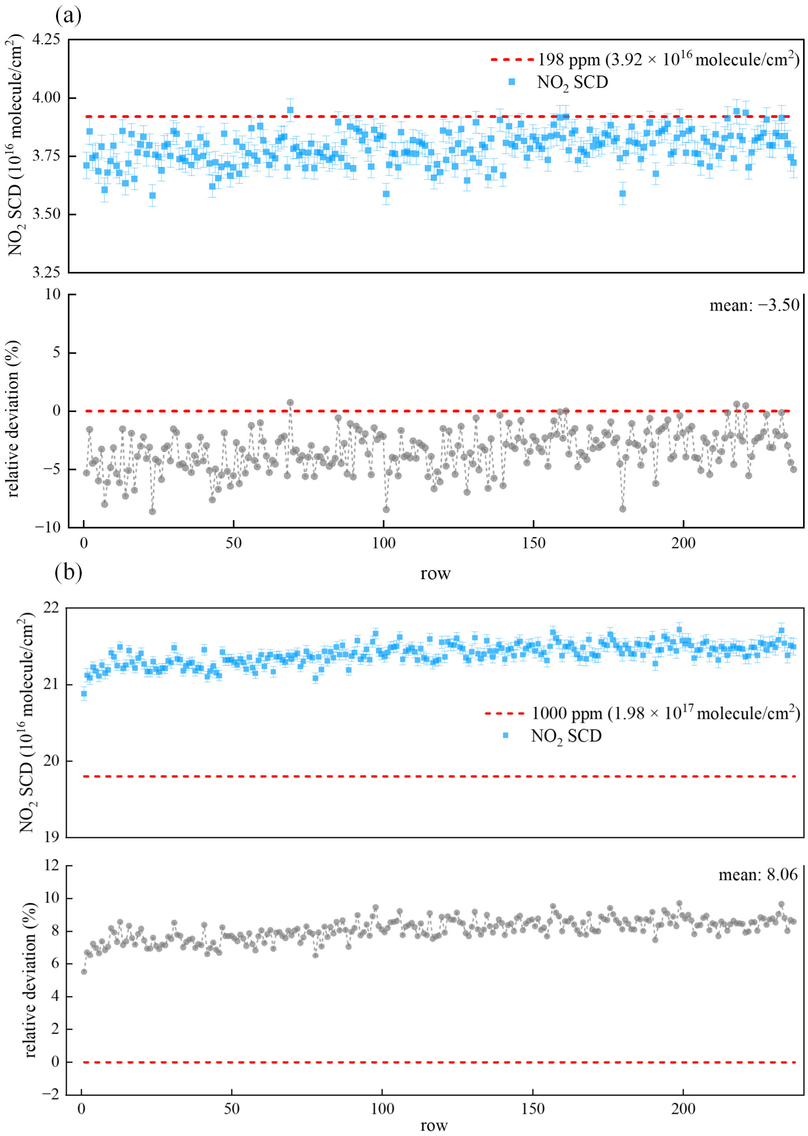

Figure 7. NO_2 SCD with fitting error and relative deviation of different spatial pixels of EMI-NL limb module with tungsten halogen lamp and NO_2 sample gas concentrations of: (**a**) 198; and (**b**) 1000 ppm.

Table 4. NO_2 gas cell measurement results of limb module.

Reference Spectral	NO_2 Gas (ppm)	Averaged NO_2 SCD (Molecule/cm^2)	Standard Deviation of NO_2 SCD	Averaged NO_2 Fitting Error (Molecule/cm^2)	Standard Deviation of NO_2 Fitting Error
tungsten halogen	198	3.64×10^{16}	2.48×10^{15}	1.48×10^{15}	4.67×10^{14}
lamp	1000	2.06×10^{17}	4.27×10^{15}	1.65×10^{15}	4.96×10^{14}
Integrating sphere	198	3.69×10^{16}	8.32×10^{14}	4.80×10^{14}	2.75×10^{13}
light	1000	2.04×10^{17}	1.70×10^{15}	7.92×10^{14}	1.10×10^{14}

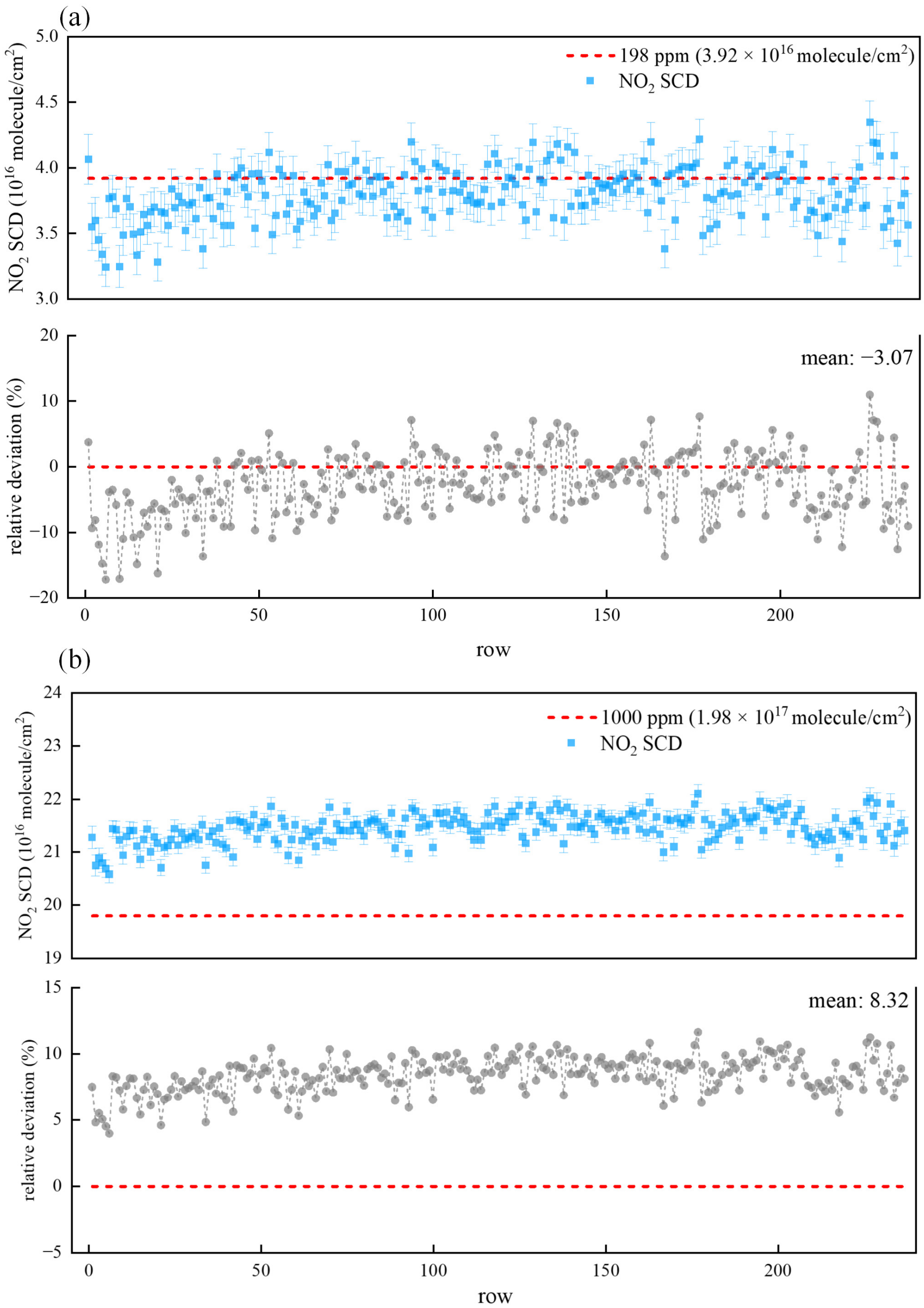

Figure 8. NO_2 SCD with fitting error and relative deviation of different spatial pixels of EMI-NL nadir module with integrating sphere and NO_2 sample gas concentrations of: (**a**) 198; and (**b**) 1000 ppm.

3.3. Results of SNR Estimation

Figure 9a–c shows the ground-based measured dark current, spectral, and SNR of the 92nd pixel of the VIS1 channel of the nadir module in the range of 430–470 nm, where the SNR fluctuated between 900 and 1400 with the integration time of 90 ms. Moreover, the nadir SNR was potentially underestimated at some wavelengths as the integration time of the measurement was somewhat short. Figure 9d–f shows the dark current, spectral, and SNR of the limb module in the 430–470 nm range of the 125th pixel of the UV2 channel. As can be seen, within the range of approximately 1000–1300 and the integration time of 0.2 s, the limb SNR meets the EMI-NL performance requirements.

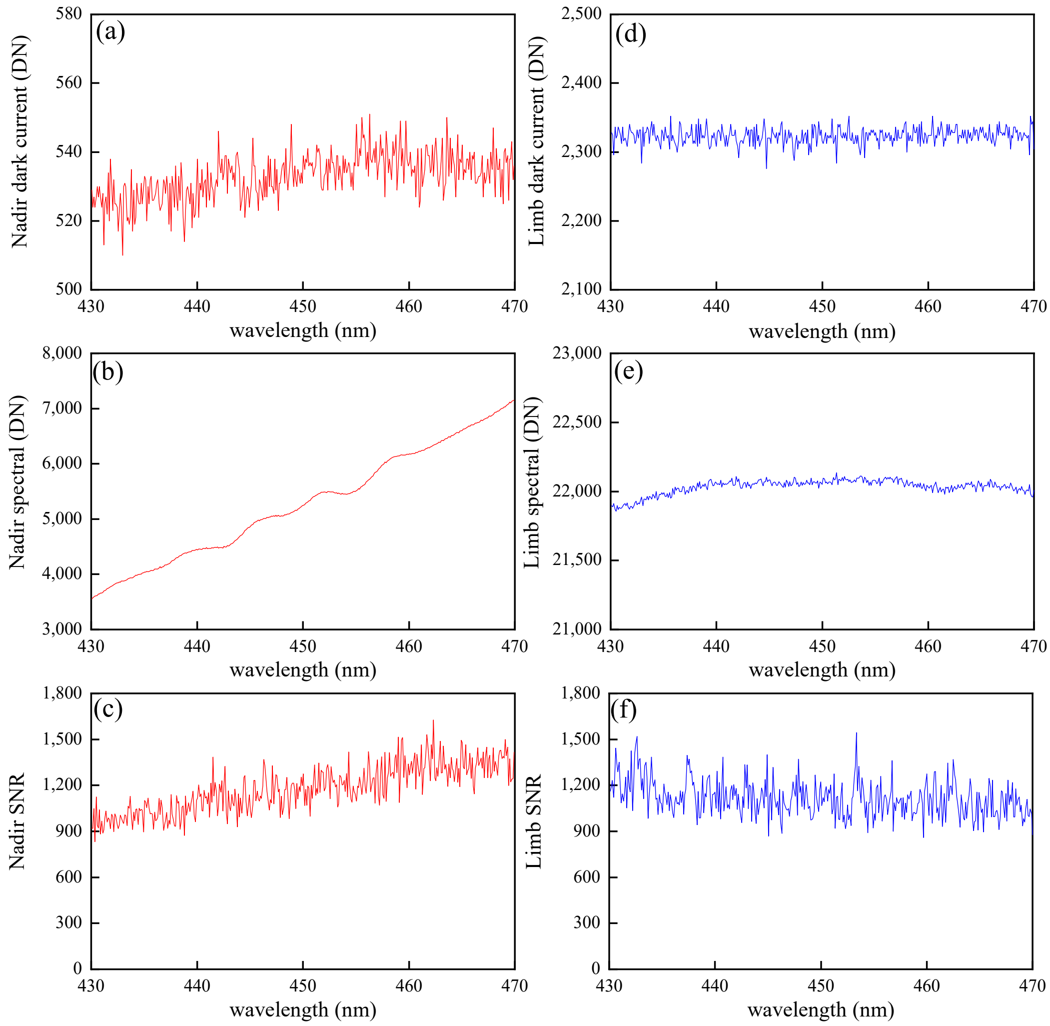

Figure 9. Ground-based measured: (**a**) dark current; (**b**) spectral; (**c**) SNR of the 92nd pixel of the VIS1 channel of the nadir module in the range of 430–470 nm; (**d**) dark current; (**e**) spectral; and (**f**) SNR of the 125th pixel of the UV2 channel of the limb module in the range of 430–470 nm.

4. Conclusions

This study used the measurements of different concentrations of NO_2 sample gas in a gas cell based on different light sources with EMI-NL in the laboratory to evaluate the trace gas monitoring capability and performance of nadir and limb modules of EMI-NL. The NO_2 SCD was retrieved by the DOAS algorithm using the measured spectrum and was compared with the estimated NO_2 SCD of the standard sample gas, while the NO_2 SCD cross-track stripe structure was obtained as well. By evaluating the monitoring ability of different spatial pixels of EMI-NL nadir and limb modules, one can acquire NO_2 SCD strips during spaceborne monitoring. Interestingly, the EMI-NL nadir and limb module pixels row pixels exhibited the same phenomenon in the experiment. More specifically, when the light source is the same, but the NO_2 sample gas concentration differs, the trends of retrieved NO_2 SCD and relative deviation for different spatial pixels are consistent. However, when the light source differs at the same NO_2 sample gas, the trends of retrieved NO_2 SCD and fitting error are inconsistent for different spatial pixels. This finding indicates that the response of spatial pixels depends on the choice of a light source, thereby inducing the inconsistencies in NO_2 SCDs and affecting the fitting error. Moreover, the experimental measurement of the limb module revealed an underestimation of NO_2 SCD when the NO_2 sample gas concentration was 198 ppm, while the NO_2 SCD was overestimated when the NO_2 sample gas concentration was 1000 ppm. Lastly, the measurement of the tungsten halogen lamp spectrum in the laboratory was used to quantify the SNR of the EMI-NL nadir and limb modules in the 430–470 nm band. The SNR evaluation demonstrated that the SNR of the nadir and limb modules exhibits variability within the range of approximately 900–1400 and 1000–1300, respectively. Overall, the SNR of the nadir module is potentially underestimated, and the integration time of the measurement could be adjusted to the most suitable time for future studies.

In general, EMI-NL performs well in laboratory measurements. The NO_2 SCDs relative error of most spatial pixels of the nadir and limb modules is within 10%, which can achieve accurate global monitoring of the NO_2 horizontal and vertical distribution. The results provide useful data for the in-orbit monitoring of EMI-NL and for the subsequent data retrieval algorithm. In future work, we could add more NO_2 sample gas concentration data points, especially those within the actual atmospheric NO_2 concentration range, so as to more clearly understand the relationship between the NO_2 SCD retrieved from the EMI-NL measured spectrum and that estimated from the NO_2 sample gas concentration, which can be used for the correction of underestimated and overestimated NO_2 sample gas concentrations in the EMI-NL limb module.

Author Contributions: Conceptualization, F.S.; Methodology, H.Z.; validation, M.Z.; resources, F.L. and L.Z.; writing—original draft preparation, T.Y.; writing—review and editing, T.Y. and H.Z. All authors have read and agreed to the published version of the manuscript.

Funding: This research was funded by National Natural Science Foundation of China, grant number 61905256, and the CASHIPS Director's Fund, grant number YZJJ2021QN05.

Data Availability Statement: The data presented in this study are available on request from the corresponding author.

Acknowledgments: The authors would like to thank the reviewers for their precious comments and suggestions.

Conflicts of Interest: The authors declare no conflict of interest.

References

1. Heath, D.F.; Krueger, A.J.; Roeder, H.A.; Henderson, B.D. The Solar Backscatter Ultraviolet and Total Ozone Mapping Spectrometer (SBUV/TOMS) for NIMBUS G. *Opt. Eng.* **1975**, *14*, 323–331. [CrossRef]
2. Burrows, J.P.; Weber, M.; Buchwitz, M.; Rozanov, V.; Ladstatter-Weissenmayer, A.; Richter, A.; de Beek, R.; Hoogen, R.; Bramstedt, K.; Eichman, K.U.; et al. The Global Ozone Monitoring Experiment (GOME): Mission concept and first scientific results. *J. Atmos. Sci.* **1999**, *56*, 151–175. [CrossRef]
3. Bovensmann, H.; Burrows, J.P.; Buchwitz, M.; Frerick, J.; Noël, S.; Rozanov, V.V.; Chance, K.V.; Goede, A.P.H. SCIAMACHY: Mission objectives and measurement modes. *J. Atmos. Sci.* **1999**, *56*, 127–150. [CrossRef]
4. Levelt, P.F.; van den Oord, G.H.J.; Dobber, M.R.; Mälkki, A.; Visser, H.; de Vries, J.; Stammes, P.; Lundell, J.O.V.; Saari, H. The Ozone Monitoring Instrument. *IEEE Trans. Geosci. Remote Sens.* **2006**, *44*, 1093–1101. [CrossRef]
5. Callies, J.; Corpaccioli, E.; Eisinger, M.; Hahne, A.; Lefebvre, A. GOME-2—Metop's second-generation sensor for operational ozone monitoring. *ESA Bull.* **2000**, *102*, 28–36.
6. Veefkind, J.P.; Aben, I.; McMullan, K.; Förster, H.; de Vries, J.; Otter, G.; Claas, J.; Eskes, H.J.; de Haan, J.F.; Kleipool, Q.; et al. TROPOMI on the ESA Sentinel-5 Precursor: A GMES mission for global observations of the atmospheric composition for climate, air quality and ozone layer applications. *Remote Sens. Environ.* **2012**, *120*, 70–83. [CrossRef]

7. Beirle, S.; Boersma, K.F.; Platt, U.; Lawrence, M.G.; Wagner, T. Megacity emissions and lifetimes of nitrogen oxides probed from space. *Science* **2011**, *333*, 1737–1739. [CrossRef]
8. Fioletov, V.E.; McLinden, C.A.; Krotkov, N.; Li, C.; Joiner, J.; Theys, N.; Carn, S.; Moran, M.D. A global catalogue of large SO_2 sources and emissions derived from the Ozone Monitoring Instrument. *Atmos. Chem. Phys.* **2016**, *16*, 11497–11519. [CrossRef]
9. Leue, C.; Wenig, M.; Wagner, T.; Klimm, O.; Platt, U.; Jähne, B. Emissions from global ozone monitoring experiment satellite image sequences. *J. Geophys. Res.-Atmos.* **2001**, *106*, 5493–5505. [CrossRef]
10. Fei, L.; Beirle, S.; Qiang, Z.; Drner, S.; Wagner, T. NOx lifetimes and emissions of cities and power plants in polluted background estimated by satellite observations. *Atmos. Chem. Phys.* **2016**, *16*, 5283–5298.
11. Lu, Z.; Streets, D.G.; de Foy, B.; Lamsal, L.N.; Duncan, B.N.; Xing, J. Emissions of nitrogen oxides from US urban areas: Estimation from Ozone Monitoring Instrument retrievals for 2005–2014. *Atmos. Chem. Phys.* **2015**, *15*, 10367–10383. [CrossRef]
12. Goldberg, D.L.; Saide, P.E.; Lamsal, L.N.; de Foy, B.; Lu, Z.; Woo, J.-H.; Kim, Y.; Kim, J.; Gao, M.; Carmichael, G.; et al. A top-down assessment using OMI NO_2 suggests an underestimate in the NOx emissions inventory in Seoul, South Korea, during KORUS-AQ. *Atmos. Chem. Phys.* **2019**, *19*, 1801–1818. [CrossRef]
13. Griffin, D.; McLinden, C.A.; Racine, J.; Moran, M.D.; Fioletov, V.; Pavlovic, R.; Mashayekhi, R.; Zhao, X.; Eskes, H. Assessing the Impact of Corona-Virus-19 on Nitrogen Dioxide Levels over Southern Ontario, Canada. *Remote Sens.* **2020**, *12*, 4112. [CrossRef]
14. Li, L.; Wu, J. Spatiotemporal estimation of satellite-borne and ground-level NO_2 using full residual deep networks. *Remote Sens. Environ.* **2021**, *254*, 112257. [CrossRef]
15. Goldberg, D.L.; Harkey, M.; de Foy, B.; Judd, L.; Johnson, J.; Yarwood, G.; Holloway, T. Evaluating NOx emissions and their effect on O_3 production in Texas using TROPOMI NO_2 and HCHO. *Atmos. Chem. Phys.* **2022**, *22*, 10875–10900. [CrossRef]
16. Zhao, M.J.; Si, F.Q.; Zhou, H.J.; Wang, S.M.; Jiang, Y.; Liu, W.Q. Preflight calibration of the Chinese Environmental Trace Gases Monitoring Instrument (EMI). *Atmos. Meas. Techn.* **2018**, *11*, 5403–5419. [CrossRef]
17. Zhang, C.; Liu, C.; Chan, K.L.; Hu, Q.; Liu, H.; Li, B.; Xing, C.; Tan, W.; Zhou, H.; Si, F. First observation of tropospheric nitrogen dioxide from the Environmental Trace Gases Monitoring Instrument onboard the GaoFen-5 satellite. *Light. Sci. Appl.* **2020**, *9*, 66. [CrossRef]
18. Xia, C.; Liu, C.; Cai, Z.; Zhao, F.; Su, W.; Zhang, C.; Liu, Y. First sulfur dioxide observations from the environmental trace gases monitoring instrument (EMI) onboard the GeoFen-5 satellite. *Sci. Bull.* **2021**, *66*, 969–973. [CrossRef]
19. Qian, Y.; Luo, Y.; Si, F.; Zhou, H.; Yang, T.; Yang, D.; Xi, L. Total Ozone Columns from the Environmental Trace Gases Monitoring Instrument (EMI) Using the DOAS Method. *Remote Sens.* **2021**, *13*, 2098. [CrossRef]
20. Yang, D.; Luo, Y.; Zeng, Y.; Si, F.; Xi, L.; Zhou, H.; Liu, W. Tropospheric NO_2 Pollution Monitoring with the GF-5 Satellite Environmental Trace Gases Monitoring Instrument over the North China Plain during Winter 2018–2019. *Atmosphere* **2021**, *12*, 398. [CrossRef]
21. Yang, T.; Si, F.; Wang, P.; Luo, Y.; Zhou, H.; Zhao, M. Research on Cloud Fraction Inversion Algorithm of Environmental Trace Gas Monitoring Instrument. *Acta Optica Sinica.* **2020**, *40*, 0901001. [CrossRef]
22. Liu, C.; Hu, Q.; Zhang, C.; Xia, C.; Yin, H.; Su, W.; Wang, X.; Xu, Y.; Zhang, Z. First Chinese ultraviolet–visible hyperspectral satellite instrument implicating global air quality during the COVID-19 pandemic in early. *Light. Sci. Appl.* **2020**, *11*, 28. [CrossRef]
23. Yang, T.; Wang, P.; Si, F.; Zhou, H.; Zhao, M.; Luo, Y.; Chang, Z. In-Flight, Full-Pixel Calibration of Reflectance in Spatial Dimension for Environmental Trace Gases Monitoring Instrument. *IEEE Geosci. Remote Sens. Lett.* **2022**, *19*, 6012205. [CrossRef]
24. Zhao, M.; Si, F.; Zhou, H.; Jiang, Y.; Ji, C.; Wang, S.; Zhan, K.; Liu, W. Pre-Launch Radiometric Characterization of EMI-2 on the GaoFen-5 Series of Satellites. *Remote Sens.* **2021**, *13*, 2843. [CrossRef]
25. Burrows, J.P.; Dehn, A.; Deters, B.; Himmelmann, S.; Richter, A.; Voigt, S.; Orphal, J. Atmospheric remote-sensing reference data from GOME: Part 1. Temperature-dependent absorption cross-sections of NO_2 in the 231–794 nm range. *J. Quant. Spectrosc. Radiat. Transf.* **1998**, *60*, 1025–1031. [CrossRef]
26. Burrows, J.P.; Richter, A.; Dehn, A.; Deters, B.; Himmelmann, S.; Voigt, S.; Orphal, J. Atmospheric remote-sensing reference data from GOME-2. Temperature-dependent absorption cross sections of O_3 in the 231–794 nm range. *J. Quant. Spectrosc. Radiat. Transf.* **1999**, *61*, 509–517. [CrossRef]
27. Bogumil, K.; Orphal, J.; Homann, T.; Voigt, S.; Spietz, P.; Fleischmann, O.; Vogel, A.; Hartmann, M.; Kromminga, H.; Bovensmann, H.; et al. Measurements of molecular absorption spectra with the SCIAMACHY pre-flight model: Instrument characterization and reference data for atmospheric remote-sensing in the 230–2380 nm region. *J. Photochem. Photobiol. A Chem.* **2003**, *157*, 167–184. [CrossRef]
28. Chehade, W.; Gür, B.; Spietz, P.; Gorshelev, V.; Serdyuchenko, A.; Burrows, J.P.; Weber, M. Temperature dependent ozone absorption cross section spectra measured with the GOME-2 FM3 spectrometer and first application in satellite retrievals. *Atmos. Meas. Techn.* **2013**, *6*, 1623–1632. [CrossRef]
29. Dobber, M.; Dirksen, R.; Voors, R.; Mount, G.H.; Levelt, P. Ground-based zenith sky abundances and in situ gas cross sections for ozone and nitrogen dioxide with the Earth Observing System Aura Ozone Monitoring Instrument. *Appl. Opt.* **2005**, *44*, 2846–2856. [CrossRef]
30. Zhang, C.; Liu, C.; Wang, Y.; Si, F.; Zhou, H.; Zhao, M.; Su, W.; Zhang, W.; Liu, X. Preflight Evaluation of the Performance of the Chinese Environmental Trace Gas Monitoring Instrument (EMI) by Spectral Analyses of Nitrogen Dioxide. *IEEE Trans. Geosci. Remote Sens.* **2018**, *56*, 3323–3332. [CrossRef]

31. Platt, U.; Stutz, J. *Differential Optical Absorption Spectroscopy: Principles and Applications*, 1st ed.; Springer: Berlin/Heidelberg, Germany, 2008; pp. 113–134.
32. Vandaele, A.C.; Hermans, C.; Simon, P.C.; Carleer, M.; Colin, R.; Fally, S.; Merienne, M.F.; Jenouvrier, A.; Coquart, B. Measurements of the NO_2 absorption cross-section from 42,000 cm^{-1} to 10,000 cm^{-1} (238–1000 nm) at 220 K and 294 K. *J. Quant. Spectrosc. Radiat. Transf.* **1998**, *59*, 171–184. [CrossRef]
33. Boersma, K.F.; Eskes, H.J.; Veefkind, J.P.; Brinksma, E.J.; Sneep, M.; Oord, G.; Levelt, P.F.; Stammes, P.; Gleason, J.F.; Bucsela, E.J. Near-real time retrieval of tropospheric NO_2 from OMI. *Atmos. Chem. Phys.* **2007**, *8*, 2103–2118. [CrossRef]
34. Boersma, K.F.; Eskes, H.J.; Dirksen, R.J.; Van, D.; Veefkind, J.P.; Stammes, P.; Huijnen, V.; Kleipool, Q.L.; Sneep, M.; Claas, J. An improved tropospheric NO_2 column retrieval algorithm for the Ozone Monitoring Instrument. *Atmos. Meas. Techn.* **2011**, *4*, 1905–1928. [CrossRef]
35. Bucsela, E.J.; Krotkov, N.A.; Celarier, E.A.; Lamsal, L.N.; Swartz, W.H.; Bhartia, P.K.; Boersma, K.F.; Veefkind, J.P.; Gleason, J.F.; Pickering, K.E. A new stratospheric and tropospheric NO_2 retrieval algorithm for nadir-viewing satellite instruments: Applications to OMI. *Atmos. Meas. Techn.* **2013**, *6*, 2607–2626. [CrossRef]